Final Report for DOE-NEER Grant DE-FG07-04ID14594

Dislocation – Radiation Obstacle Interactions: Developing Improved Mechanical Property Constitutive Models

B.D. Wirth
Nuclear Engineering Department
University of California, Berkeley
Berkeley, CA 94720-1730

and

Ian M. Robertson, co-PI
Department of Materials Science and Engineering
University of Illinois, Urbana-Champaign
1304 West Green St
Urbana, IL 61801

November 2007

Work supported by the Office of Nuclear Energy, Science and Technology, U.S. Department of Energy under Contract No. DE-FG07-04ID14594.

Contents

I. Executive Summary

Radiation damage to structural and cladding materials, including austenitic stainless steels, ferritic steels, and zirconium alloys, in nuclear reactor environments results in significant mechanical property degradation, including yield strength increases, severe ductility losses and flow localization, which impacts reliability and performance. Generation IV and advanced fuel cycle concepts under consideration will require the development of advanced structural materials, which will operate in increasingly hostile environments. The development of predictive models is required to assess the performance and response of materials in extreme Gen IV reactor operating conditions (temperature, stress, and pressure), to decrease the time to rapidly assess the properties of new materials (e.g., new alloys, nanostructured materials) and insert them into technological applications (Gen IV and Advanced Fuel Cycle Operations). In this project we focus on identifying the controlling mechanisms of dislocation interactions with a range of obstacles commonly produced in material microstructures under irradiation (stacking fault tetrahedron and dislocation loops, and radiation-induced precipitates) through a combination of atomistic modeling and dynamic in situ and static ex-situ transmission electron microscopy experiments. Molecular dynamics was used to determine time evolution dynamics. Correlation of the simulation and experimental results provide information of the governing dynamics that are inaccessible to either approach alone, but that dominate the macroscopic mechanical response. The material systems investigated focused on copper and iron-based alloys, representative of the most-promising austenitic and ferritic steels for advanced reactor applications, although the findings are likely to be generic to many material systems.

The results are able to determine the obstacle strengths, including the observation of new interaction/strengthening mechanisms, and provide insight into the localized deformation in the form of defect free channels observed in irradiated structural materials. Molecular dynamics simulations of the interaction between edge, screw or mixed dislocations and a SFT show that the SFT is a strong barrier to dislocation motion. Further, these observations lead to the conclusion that dislocation channel formation is much more complicated than defect absorption in a single interaction, and may result from a combination of i) decreased defect cluster size due to shear, ii) partial absorption leaving isolated vacancies and smaller defect clusters of presumably reduced obstacle resistance, and iii) partial to complete absorption and the subsequent dragging and re-emission of defect clusters at a different location. The study of dislocation – precipitate interactions has revealed a new dislocation interaction mechanism with coherent precipitates that can explain the strong irradiation hardening observed in reactor pressure vessel steels. Ultimately, the dislocation-radiation obstacle interaction rules will be incorporated in higher length scale models to predict the post-yield constitutive properties of irradiated materials required for the design of advanced material systems for advanced Nuclear technology.

II. Background and Research Approach

The materials for use in Generation IV and Advanced Fuel Cycle Initiatives present significant material challenges. These materials will be required to operate in higher temperatures and radiation fields, will be subjected to more extreme cyclic variations of temperature and applied stress, and will be exposed to more corrosive coolants than in current generation reactors. It is well established that neutron radiation damage to structural and cladding materials in current nuclear environments (Generation I and II reactor systems) produces significant mechanical property degradation.[1-11] However, despite the extensive effort which has produced a significant body of knowledge regarding the macroscopic degradation, we lack the physically-based models that are capable of predicting this degradation and materials failure. This is particular apparent as we attempt to predict the material response in the elastic-plastic regime. A consequence of this lack of predictive capability is that rapid assessment on new candidate alloy systems is hindered.

The development of predictive models requires input of the essential features of the dominant deformation processes over multiple length and time scales. This proposal utilizes the latest advances in computational science and analytical experimental techniques to develop a fundamental understanding of dislocation interactions with the obstacles commonly observed in irradiated materials (e.g., dislocation loops, voids, helium bubbles, stacking fault tetrahedra, and radiation-induced precipitates). Ultimately, the dislocation-obstacle behavior gleaned from this study will be incorporated in higher length scale models to predict the post-yield constitutive

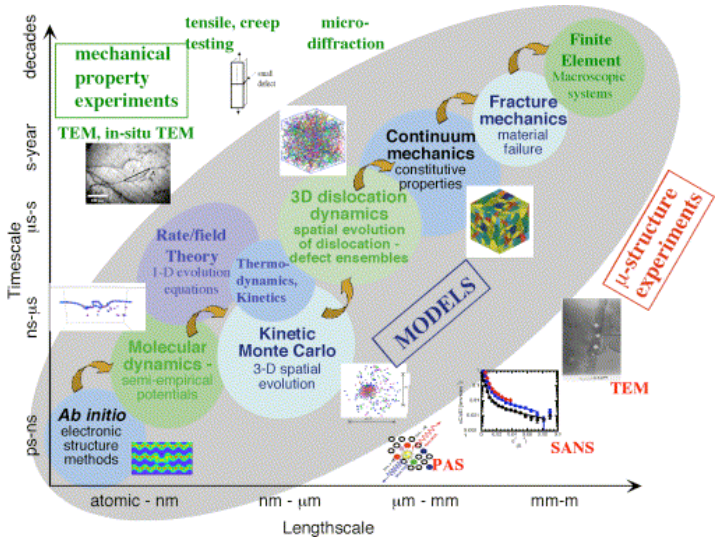

Figure 1. Illustration of an integrated experimental and computational approach to the multiscale investigation of materials behavior in the fusion environment. The central part of the figure describes a hierarchical approach based on passing information or parameters, and connecting key mechanisms (denoted by arrows), starting from the electronic/atomic up to structural length and time scales. A number of microstructural characterization techniques important for validating model predictions are represented on the lower right side, including the techniques of positron annihilation spectroscopy (PAS), small angle neutron scattering (SANS) and transmission electron microscopy (TEM). The upper left side of the diagram represents experimental techniques to measure mechanical properties.[1]

properties of irradiated materials. The program is therefore divided into an experimental and a computational component with the former being conducted at the University of Illinois under the direction of Ian Robertson and the latter at the University of California at Berkeley under the direction of Professor Brian Wirth

Figure 1 provides a schematic illustration of one of these multiscale approaches to modeling the plastic response of metals.[1] The ultimate goal is to model the behavior at different length and time scales within one grand multiscale scheme. Within this approach, first principal simulations yield the interatomic interactions, molecular dynamics computer simulations determine interatomic processes on the Ångstrom length scale, dislocation dynamics for long-range interactions on the micrometer length scale. This then provides the basis on which to develop continuum finite element models of deformation and fracture mechanics which are used to predict material responses. The overlapping circles are indicative of length and time scales overlaps between the different methods. Also, shown in the figure are experimental approaches that can provide information at appropriate length and time scales. An integrated approach that combines experiments and modeling is seen as key to the development of physically-based predictive models of the material properties. In this program our approach is to use electron microscopy, especially the dynamic testing in the electron microscope, along with the molecular dynamics computer simulation to reveal the atomistic processes responsible for controlling the interaction between dislocations and irradiation produced defects.

To illustrate how this combined approach can lead to predictive model we have previously considered how defect-free channels are created by the sweeping action of dislocations and how this action results in a loss of ductility, the increase in the yield and tensile strength, and the development of the apparent yield point in FCC type materials in irradiated materials. The *in situ* TEM studies showed that the dislocation sources were grain boundaries and stress concentrators not pre-existing dislocations, that defects were not annihilated by the interaction with just one dislocation, that the obstacle strength for any defect is not constant but is variable and depends on the geometry (size of the defect, position of impact of the dislocation on the defect, defect type etc.) of the interaction.[12,13] A crystal plasticity model based on the dispersed-barrier hardening concept was developed that included the effect of decreasing the effective hardness of the radiation defects as the mobile dislocations shear them and the preexisting dislocations do not contribute significantly to the total plasticity.[14] Another critical concept that was introduced was that the resistance to dislocation glide is proportional to the sum of the obstacle densities rather than the sum of individual resistance contributions. Figure 2 shows the stress-strain curves generated as a function of defect density – neutron exposure. The results show striking similarities with experimental observations.

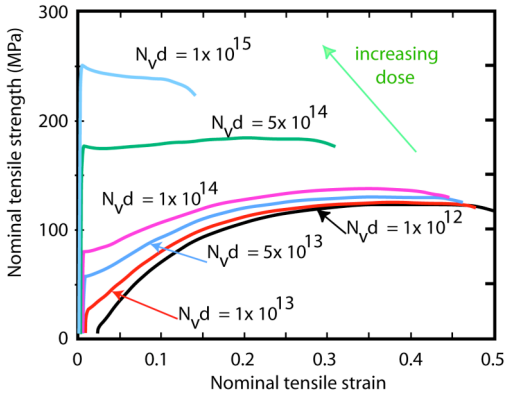

Figure 2. Predictions of the stress-strain relation as a function of increasing dose.

Molecular dynamics computer simulations have been used to investigate the interaction of an edge, screw or mixed dislocation with a perfect stacking fault tetrahedron or partially dissociated Frank loops in FCC Cu, and to investigate the interaction of screw or edge

dislocations with coherent copper precipitates in BCC Fe-Cu alloys. The molecular dynamics simulations use the embedded atom method potential developed by Mishin[14] to describe FCC Cu, and developed by Ackland and co-workers[15] for the BCC Fe-Cu system.

The simulation cell with FCC crystalline structure consists of orientations with x=[$\bar{1}$11], y=1/2[110] and z=1/2[1$\bar{1}$2] is used. For a screw dislocation, a simulation cell with 31.4 nm in x, 22.5 nm in y and 44.3 nm in z direction, which is (50x88x100) in unit cells and contains 2.6x10^6 atoms is used. For an edge dislocation, a simulation cell with 31.4 nm in x, 25.5 nm in y and 39.0 nm in z direction, which is (50x100x88) in unit cells and contains 2.6x10^6 atoms is used. For a mixed dislocation, a simulation cell with 12.5 nm in x, 22.5 nm in y and 35.3 nm in z direction, which is (20x88x80) in unit cells and contains ~0.84x10^6 atoms is used. Thus, the dislocation line length and inter-particle (SFT) spacing is 22.5 nm for a screw and a mixed dislocation, while 39.0 nm for an edge dislocation.

The screw dislocation of burger's vector (*b*) 1/2[$\bar{1}\bar{1}$0] is introduced using the elastic isotropic displacement field. The edge dislocation of *b* = 1/2[$\bar{1}\bar{1}$0] is introduced by removing two [110] half planes. The 60 degree mixed dislocation of *b* = 1/2[0$\bar{1}$1] is introduced by introducing an 1/4[$\bar{1}\bar{1}$0] screw dislocation in y direction and removing three [1$\bar{1}$2] half planes ($\frac{1}{2}[0\bar{1}1] = \frac{1}{4}[\bar{1}\bar{1}0] + \frac{1}{4}[1\bar{1}2]$). Perfect and truncated SFT were introduced by inserting triangular, or truncated triangular, vacancy platelets containing 45 to 153 vacancies, which form SFT, truncated SFT, or overlapping SFT with edge length from 2.5 to 4.6 nm, compared to the experimentally observed value of 2.5±0.5nm.

Periodic boundary conditions are used in the y and z directions, while the x direction is a free surface, subject to an applied shear surface traction. In the case of a screw dislocation, the periodic boundary condition in the z direction is modified by shifting atomic positions by ±b/2 in the y direction to ensure the continuity of the [110] plane across the periodic boundary in the z direction, following the work of Rodney[16]. In the case of a mixed dislocation, the amount of shift in the y direction is set to ±b/4. The simulation cell was equilibrated for 50 ps at T = 100 K using an NVE ensemble. Following equilibration, a shear stress of 300 MPa is applied to the system by adding forces parallel to the corresponding Burger's vector direction to the atoms on the free surface x.

The visualization of the interaction process of the SFT and dislocation are performed using the common neighbor analysis[17]. This method identifies the local atomic structure as a sequence of three integers (ijk) for each first nearest neighbor pairs (root pair). The first integer (i) is the number of nearest neighbor atoms shared in common by the root pair. The second (j) is the number of nearest neighbor bonds among the common neighbors. The third integer (k) is the length of continuous nearest neighbor bonds among the common neighbors. For example, the FCC structure gives only 421, while the hexagonal closed packed (HCP) structure gives equal amounts of 421 and 422. Using this information, the atoms are color coded to represent different local order. The yellow atoms are atoms in HCP structure, thus corresponding to stacking faults, and blue atoms are neither FCC nor HCP, corresponding to dislocation or stair-rod partial dislocation cores.

The simulation cell for studying dislocation – precipitate interactions in the BCC Fe-Cu system consists of a cell, bounded by {112}, {111} and {110} faces in *X*, *Y* and *Z* directions, respectively. The cell dimensions are approximately 14 x 25 x 28 nm (*X*, *Y* and *Z* directions) and contain 840,000 atoms. Periodic boundary conditions are applied in the *Y* and *Z* directions. The *X*

surface is initially free, but is subject to a constant (equal and opposite) surface traction in the [111] direction on the atoms in the outermost $(\bar{1}\bar{1}2)$ and $(11\bar{2})$ surfaces following equilibration to apply a shear stress of 500 to 2,000 MPa to drive dislocation motion. A coherent bcc Cu precipitate, with diameter from 1 to 4 nm, is placed at the center of the cell about 6 nm away from the screw dislocation, which is introduced based on the continuum elastic displacement field. Before applying a shear stress, the cell is equilibrated for 50 ps at 10 K. A time step of 1 fs is used throughout the simulations.

III. Results and Discussion

A. Dislocation – SFT Interaction

The interactions between edge, screw or mixed dislocations with SFT have been investigated using MD simulations. The resulting SFT structures immediately after the interaction are almost identical, even though the nature of the dislocation and sequence of events during the interaction processes are different. As shown in Fig. 3, the SFT is effectively decomposed into a smaller perfect SFT and a truncated base regardless of the character of the dislocation with which it interacted. The truncated base is a sessile defect, composed of 4 Shockley and 6 stair-rod partial dislocations.

Shortly after the detachment of the trailing partial, which occurs by an Orowan-like mechanism, additional dislocation reactions occur between the small perfect SFT and the truncated base, resulting in transformation to a sheared SFT structure containing ledges. These structures are shown in Fig. 4. The ledges shown in (a) and (c) are consistent with the anticipated interstitial (I) and vacancy (V)-ledges formed as a result of shear of the SFT. Notably, the ledges are often unstable and can self-heal through dislocation glide reactions, as expected from the relatively high ledge energies.

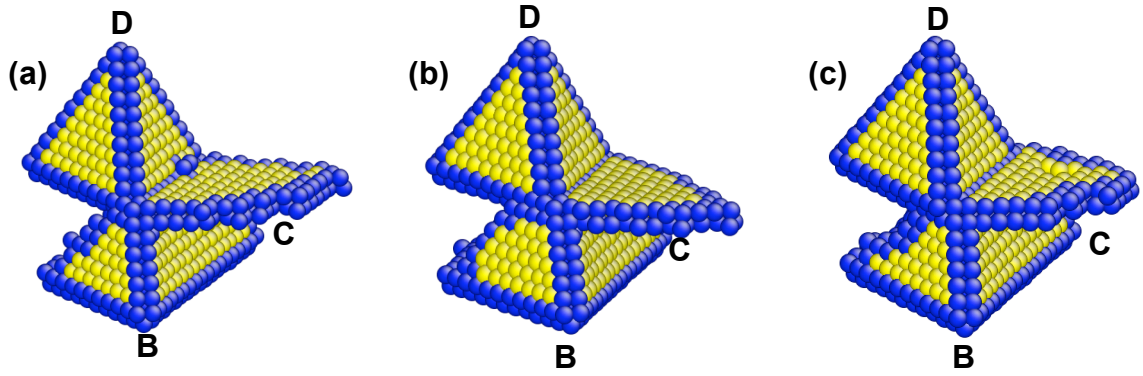

Figure 3. The structure of SFT immediately after the detachment of trailing partial (dA) when the gliding dislocation is (a) Screw dislocation (b=BA) (b) Edge dislocation (b=BA) (c) Mixed dislocation (b=CA). The dA tailing partial detached by an Orowan-like mechanism, leaving dA segment on the SFT

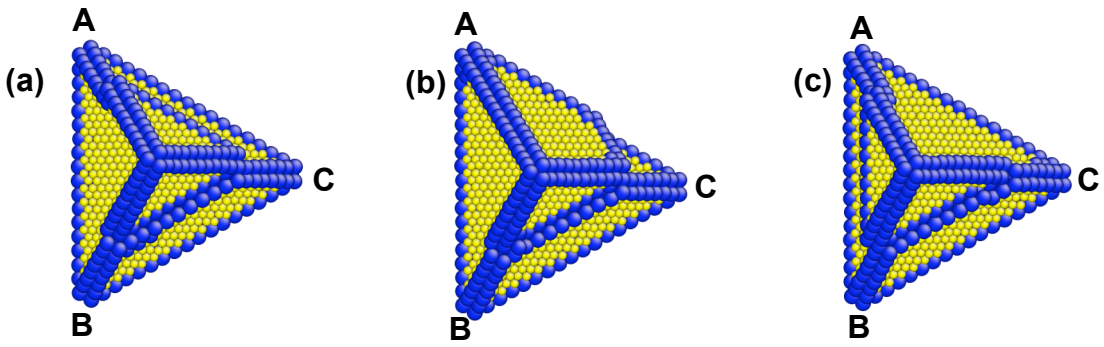

Figure 4. The structure of SFT 5ps after the detachment of trailing partial (dA) when the gliding dislocation is (a) Screw dislocation (b=BA) (b) Edge dislocation (b=BA) (c) Mixed dislocation (b=CA). Note that along the burgers vector, no ledges are formed on the sheared SFT surface.

The interaction mechanisms observed in the MD simulations are summarized as below:

III.A.1. Screw dislocation interacting with an SFT (Figure 5)

The dissociated partial dislocations (Bδ and δA) of the screw dislocation ($\vec{b} = BA$) intersect with the SFT as they glide on the (d)-plane. Initially, the segment bounded by the SFT constricts on the inclined (c) surface of the SFT. Subsequently, the screw dislocation re-dissociates on the (c)--plane as Bγ and γA, following cross slip (Fig. 5(a)). Immediately thereafter, γA moves towards the base, eliminating the stacking fault on the lower portion of the SFT. When γA meets the stair-rod γβ on the AD edge and the dg stair-rod on the AB edge, it forms βA and δA Shockley partials on the (b) and (d)-planes, respectively. These two Shockley partials move on the (b) and (d)-planes, eliminating the stacking faults of the SFT on the (b) and (d)-planes (Fig. 5(b)).

As a result of the applied shear stress, the screw partials on the (d)-plane outside of the SFT bow around the SFT. Around the constriction point E, Bδ glides inside the SFT and forms δγ on the (c)- plane, which is an edge of a smaller SFT. At the same time, the trailing δA partial glides along with Bδ and forms δβ by a reaction with βA (δA+Aγ→δb) on the (b)-plane, which is also an edge of a smaller SFT (Fig. 5(c)). At the constriction point F, Bα is formed on (a)-plane and reacts with the leading Bδ partial, forming δα stair rod dipole. The trailing δA is detached from the truncated base by an Orowan-like mechanism, thus leaving the δA Shockley partial attached to the δα stair rod of the truncated base.

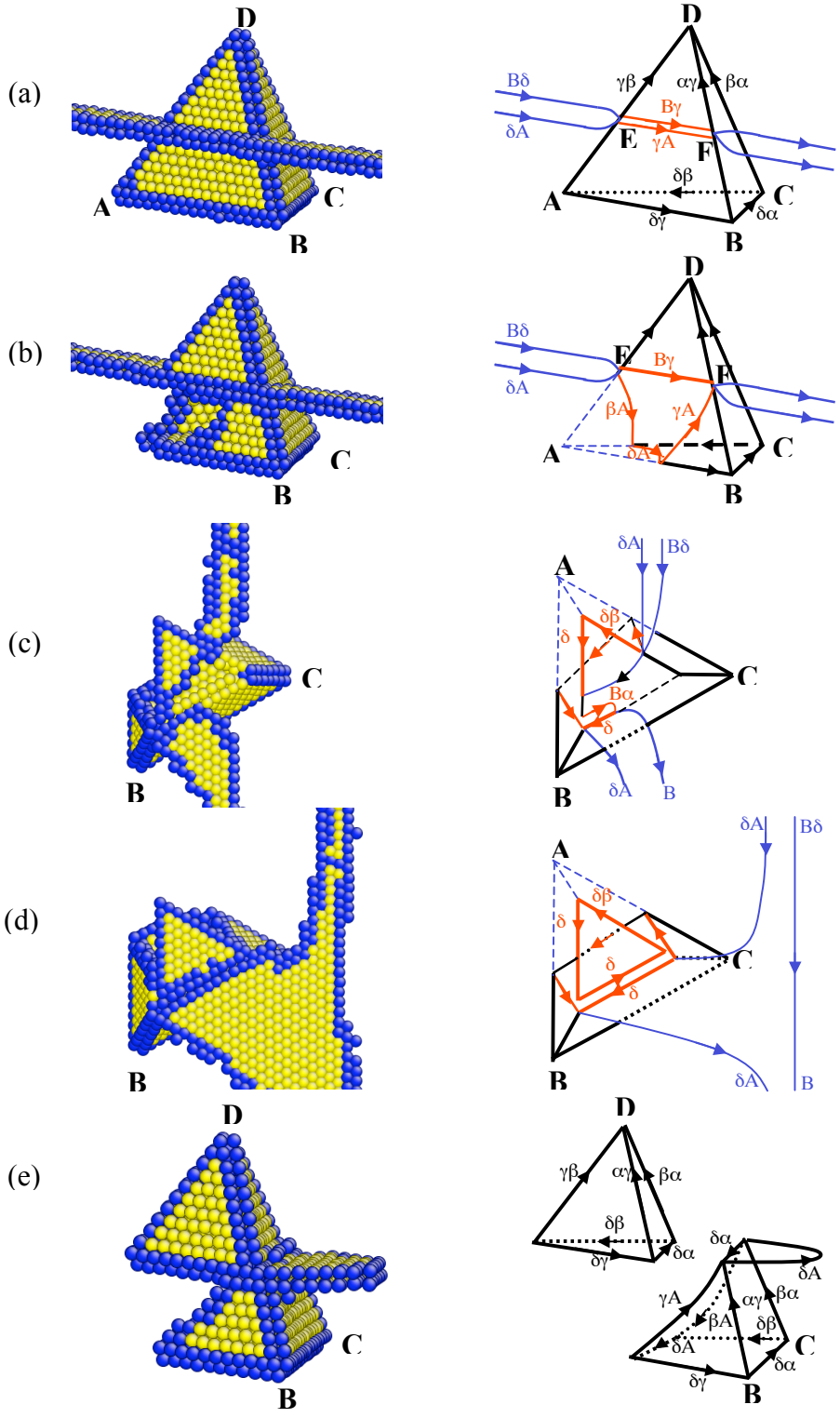

Figure 5. Screw dislocation (b=BA) passing the SFT at applied shear stress 300MPa.

III.A.2. Edge dislocation interacting with an SFT (Figure 6)

The leading Bδ partial is constricted on the (b)-face of the SFT as the dissociated partials move toward the SFT (Fig 6a). Upon continuous applied shear stress, the stair-rod partials of SFT around the point A dissociate into Shockley partials by a reverse Silcox-Hirsch process. As the SFT opens up starting from point A, the Bδ glides inside of the SFT while dragging the γA and βA Shockley partials (Fig 6b). Then, the trailing partial δA moves towards the SFT and reacts with the Shockley partials γA and βA, forming stair-rod partials δβ on (b)-face and δγ on (c)-plane, respectively. The resulting stair-rod partials are edges of the smaller SFT.

As both partials constrict on the (a)-face of the SFT, Bα is formed on (a)-plane and reacts with the leading Bδ partial, forming a δα stair rod dipole. The trailing δA detaches from the truncated base by an Orowan-like mechanism, thus leaving a δA Shockley partial attached to the δα stair rod of the truncated base.

III.A.3. Mixed dislocation interacting with an SFT (Figure 7)

The dissociated partial dislocations (Cδ and δA) of the mixed dislocation ($\vec{b} = CA$) intersect with the (c)-face of the SFT as they glide on the (d)-plane. They first constrict on the (c)-face of the SFT, then dissociate into Shockley partials Cδ and γA and the stair-rod partial δγ. δγ forms an edge of the small SFT, while the γA starts to move toward the base of the SFT, eliminating the stacking faults and edges around the point A. The reaction of γA is similar to that observed for the screw dislocation.

As the leading Cδ cuts through the SFT, the trailing δA forms δβ on the (b)-face of the SFT, producing an edge of the small SFT. When both partials constrict on the (a)-plane, Cα is formed. Cα reacts with Cδ, forming a δα stair-rod dipole. Identical to the previous two cases, the trailing δA detaches from the truncated base by an Orowan-like mechanism, thus leaving a δA Shockley partial attached to the δα stair rod of the truncated base.

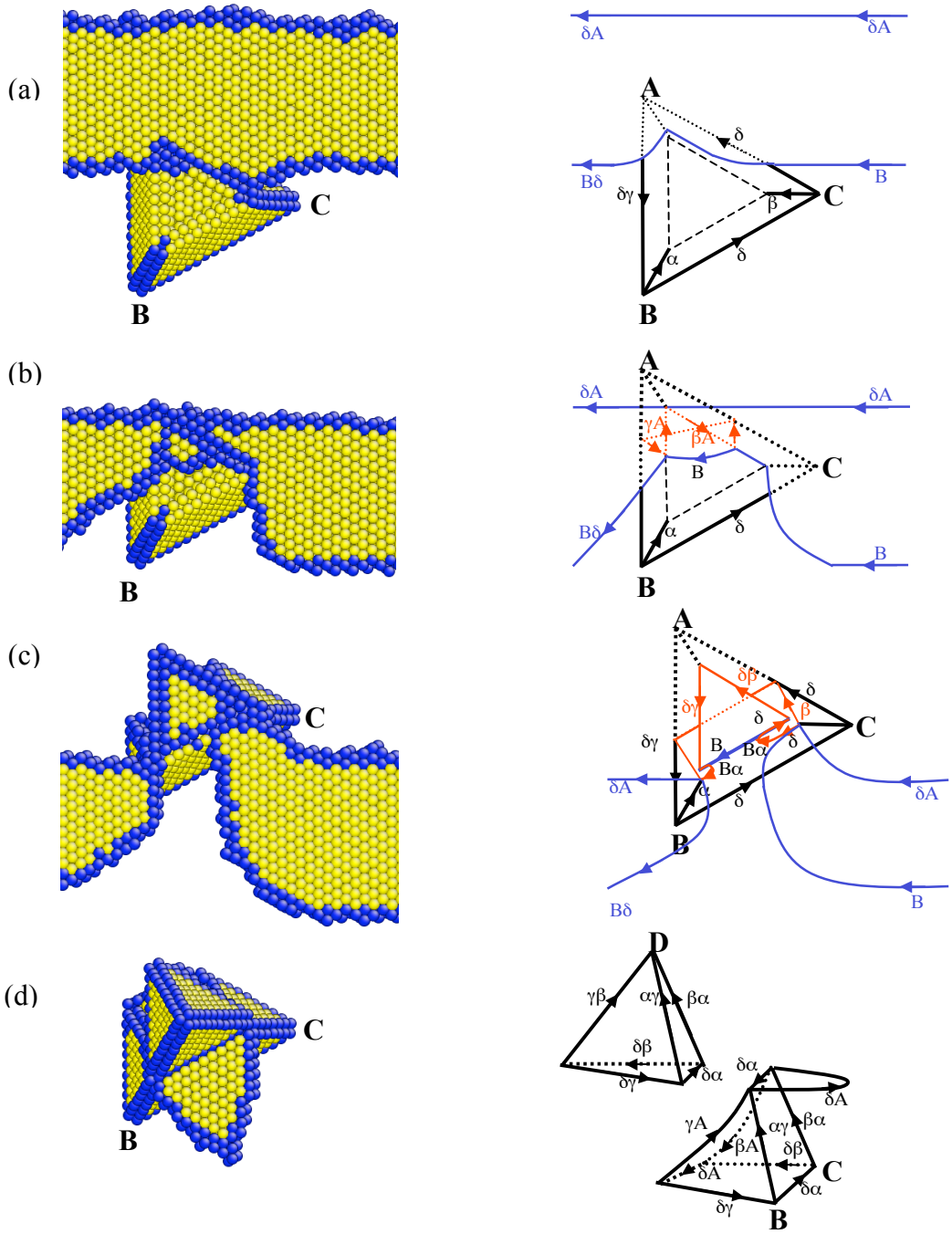

Figure 6. Edge dislocation (b=BA) passing the SFT at applied shear stress 300MPa.

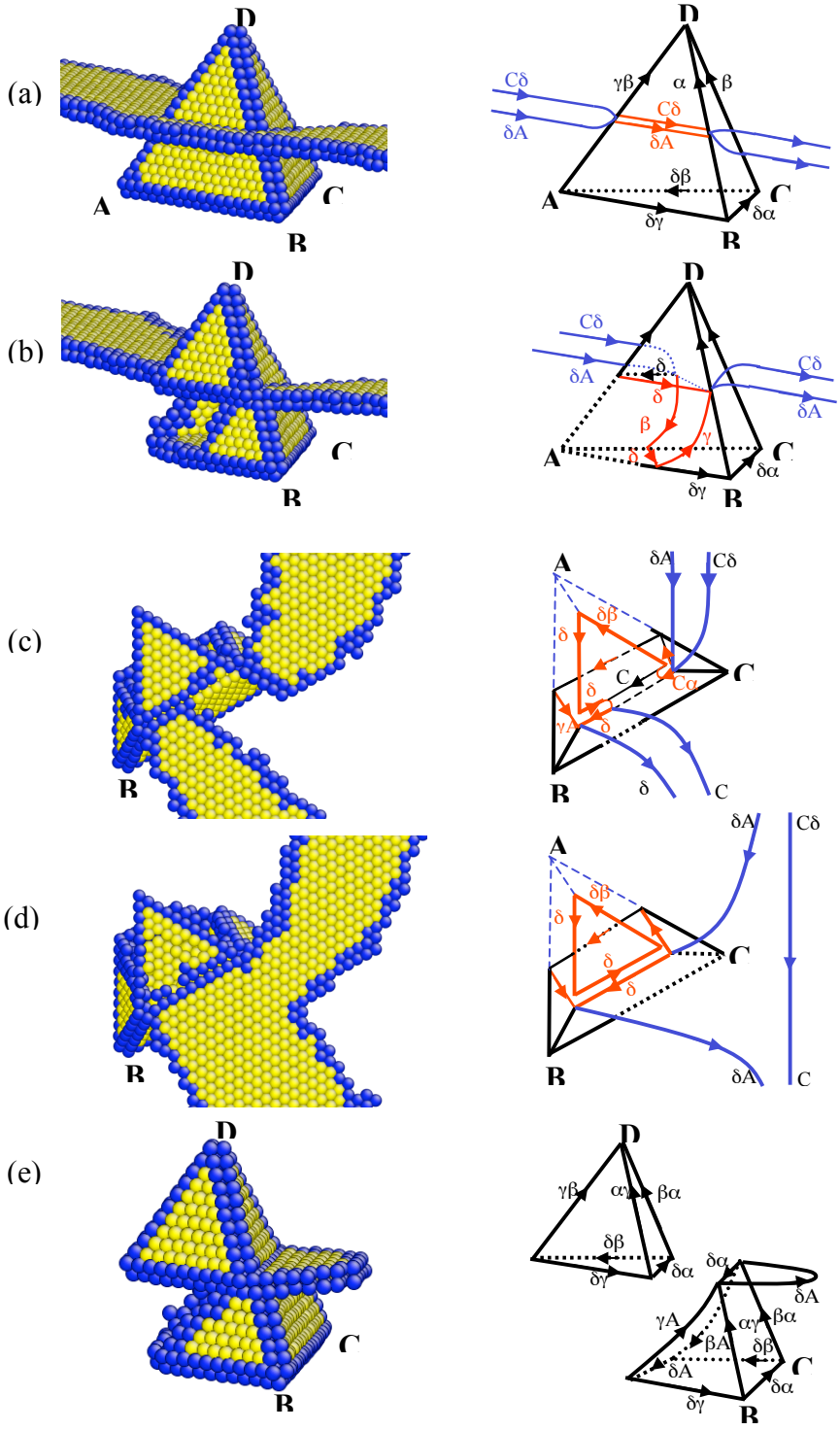

Figure 7. 60 degree mixed dislocation (b=CA) passing the SFT at applied shear stress 300MPa.

B. Dislocation – Truncated SFT/Frank loop Interaction

A series of simulations using different interaction geometry have been performed to study the interaction of an edge or screw dislocation with a truncated SFT, also known as a partially dissociated Frank loop. In all simulations, the truncated platelet of vacancies was introduced on the $(1\bar{1}\bar{1})$ plane with a dislocation glide plane of $(\bar{1}11)$.

III.B.1 Screw dislocation interacting with a truncated SFT (Figure 8)

Figure 8 shows a series of MD simulation snapshots (in $[\bar{1}11]$ projection) of the interaction between a screw dislocation and a 98-vacancy truncated SFT/partially dissociated Frank loop under an incrementally increasing applied shear stress. Fig. 8a shows the dislocation-defect configuration after 40 picoseconds at 100K with no applied a stress. Figures 8 (b), (c) and (d) show configurations with a shear stress of 100MPa. Figure 8 (e) and (f) show the configuration with a stress of 200MPa and Figures 8 (g) and (h) are at an applied stress of 300 MPa. The 100, 200 and 300 MPa shear stresses were applied for 30, 20ps and 20ps, respectively. Initially, the dislocation remains pinned by the super-jogs (or helical turn), even with the application of an applied shear stressalthough the super-jog segments fluctuate (migrate) along the dislocation line. After the application of a shear stress of 300Mpa for about 3ps, the dislocation finally detaches from the defect cluster (Fig. 8 (h) and (i)). The resulting defect is still a truncated SFT, which has rotated 60° compared to the initial position and been moved about 12 nm along the dislocation line. Thus, despite absorption of the truncated SFT, the dislocation ultimately detaches from the defect under an applied shear stress, and leaves behind the same truncated SFT defect structure as initially encountered.

III.B.2 Edge dislocation interacting with truncated SFT

Figure 9 shows a series of MD simulation snapshots when an edge dislocation glides on the mid-plane between the base and top portion of the truncated SFT, in which the resulting interaction is quite sensitive to the contact geometry. Interactions between the edge dislocation and truncated SFT at other heights (e.g., base of the truncated SFT) generally produced a shear step in the faulted defect structure. Configurations associated with initially placing the truncated vacancy platelet on either the $(1\bar{1}\bar{1})$ plane or the (111) plane have been investigated. Figure 9(a) and 9(c) shows the configuration of the truncated SFT on either the $(1\bar{1}\bar{1})$ or the (111) plane following 20 ps at 100 K without applied stress, respectively. At this time, a 100 MPa shear stress is applied and the dislocation begins to move toward the defect structure. When the initial vacancy platelet is on the $(1\bar{1}\bar{1})$ plane (Fig. 9(a)), the edge dislocation is strongly pinned (blocked) by the defect as shown in Figure 9(b). The dislocation remains pinned as the applied stress is increased up to 500MPa, with an increment of 100MPa per 20ps. On the other hand, when the initial vacancy platelet is on the (111) plane, as shown in Figure 9(c), the dislocation partially absorbs the defect by forming super jog segments and leaves a smaller defect and several small vacancy clusters behind (Fig. 9(d)). The result of the partial absorption of the truncated SFT by the edge dislocation is that the dislocation now has a reduced mobility associated with the superjog pair, and the defect cluster has been broken down into two smaller vacancy defect clusters and an isolated vacancy.

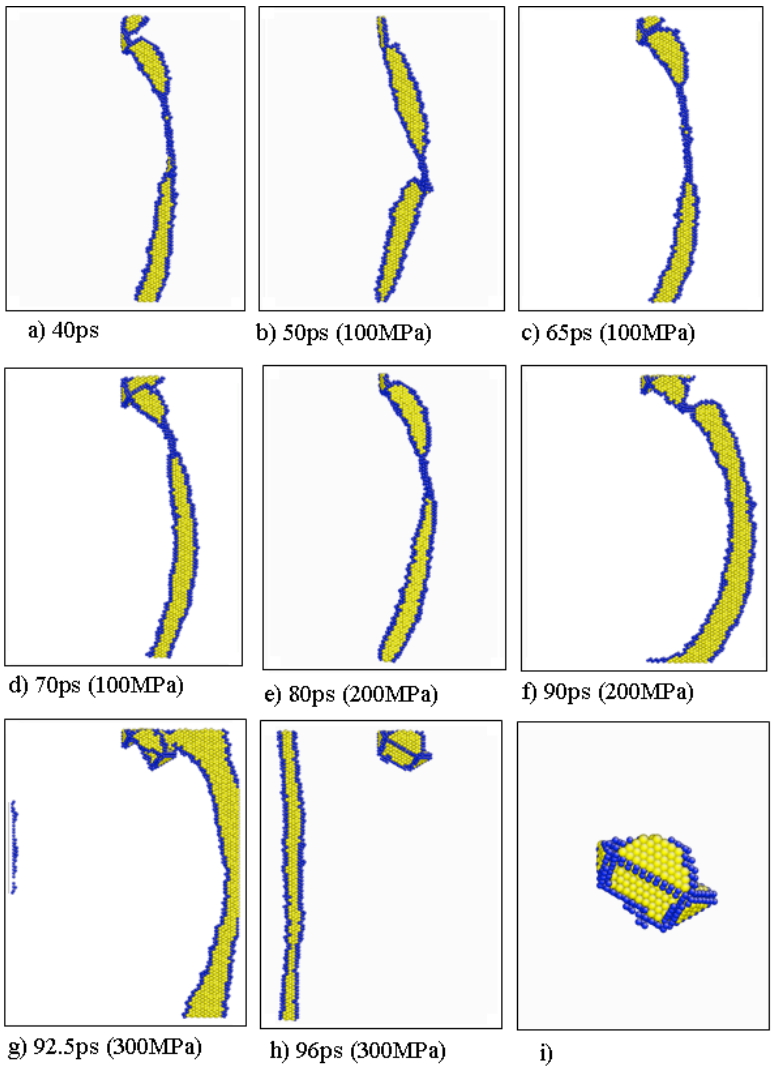

Figure 8. Snapshots in time and [$\bar{1}11$] projection from an MD simulation at 100 K, showing the sequence of events during the interaction of a screw dislocation and a truncated SFT with an applied shear stress. (a) Configuration of the partially absorbed defect cluster and screw dislocation with a helical turn following 40 ps at 100K without applied stress. Observed evolution with an applied shear stress of (b-d) 100 MPa and (e-f) 200 MPa (g-h) Observed evolution at an applied stress of 300 MPa as the screw dislocation detaches and (i) the resulting partially dissociated Frank loop defect structure.

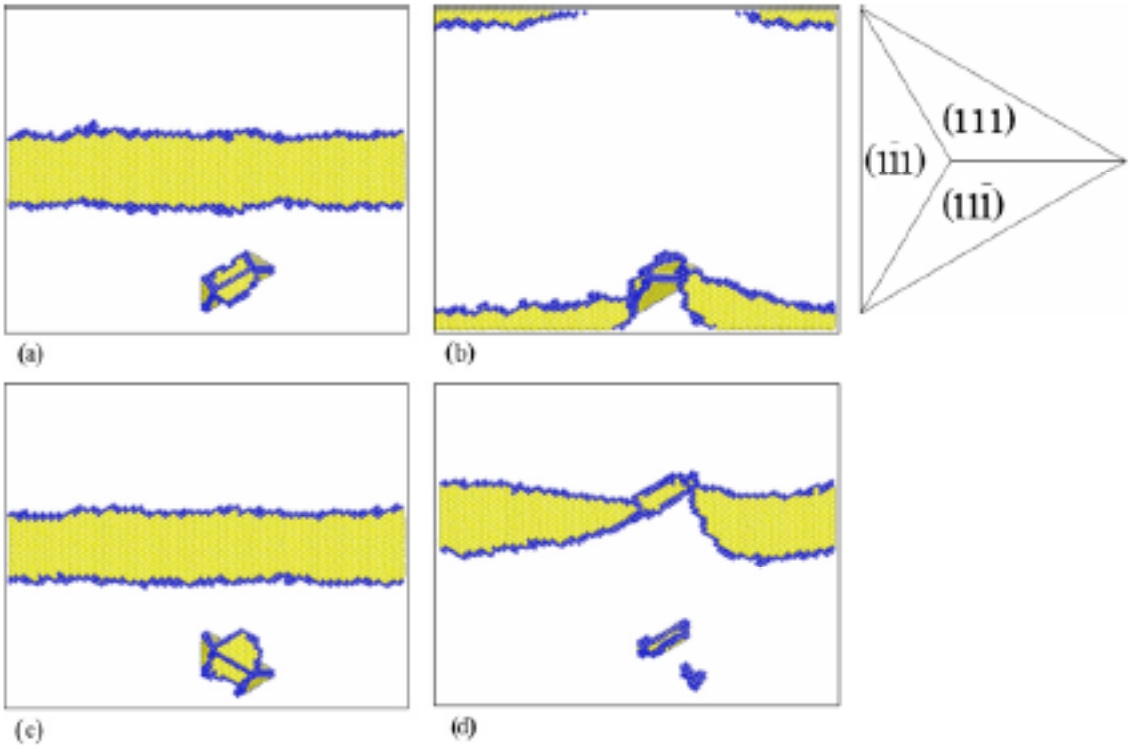

Figure 9. Snapshots in time and [$\bar{1}$1 1] projection from an MD simulation at 100K, showing the interaction of an edge dislocation and a 98-vacancy truncated SFT in different configurations under a 100MPa shear stress. Figure a) and c) show the initial configuration. Figure b) and d) show the configuration after applying a shear stress. On the right, schematic [$\bar{1}$1 1] projection of the tetrahedron of Thomson is showing the different planes.

C. Dislocation – Precipitate Interaction

Figure 10 presents snapshots in time from an MD simulation of the interaction between a screw dislocation and a 2.5 nm diameter coherent bcc Cu precipitate with an applied shear stress of 1,000 MPa (left side), and the corresponding atomic configurations of the precipitate (right side). Fig. 10b shows the configuration 27 ps after applying the shear stress, when the screw dislocation begins to intersect and slightly penetrate the precipitate. However, the screw dislocation is unable to glide further within the precipitate and remains pinned. The dislocation line outside the precipitate continues to glide forward and loops around the precipitate until reaching a critical bowing angle of nearly 0 degrees (Fig. 10c). As the dipole segments of the dislocation strongly interact and annihilate on the departure (left) side of the precipitate, the screw dislocation is able to detach from the precipitate, leaving an Orowan loop. The screw dislocation continues to move forward away from the precipitate and the glide loop remains stable, although some dislocation loop segments partially penetrate the precipitate (Fig. 10d).

For comparison, an MD simulation of the interaction between an edge dislocation and a 2.5 nm diameter bcc Cu precipitate reveals little resistance of the precipitate to dislocation bypass by the shear mechanism, although the results are not presented here. Thus the precipitate resistance is significantly larger to the motion of a screw than an edge dislocation, and presumably responsible for the different interaction and detachment mechanism, i.e. Orowan

looping for the screw and shear for the edge dislocation. MD simulations of screw dislocation interaction with 1.0, 1.8 and 4 nm bcc Cu precipitates reveal that the Orowan mechanism also occurs for the 4 nm precipitate, whereas the shear mechanism operates for the smaller ones (1.0 and 1.8 nm).

As the screw dislocation approaches the 2.5 nm (and also 4 nm) diameter precipitate, a significant fraction of Cu atoms within the precipitate transform from the original bcc structure. The majority of the transformed Cu atoms have an hcp structure, although some Cu atoms within a single $(1\bar{1}0)$ layer transform into an fcc structure, as shown in Fig. 10b. The transformation into the hcp structure is consistent with the shear instability of bcc Cu indicated by Ackland *et al*.[15], which corresponds to the bcc-to-hcp transformation. It is important to note that the transformation nucleates within the precipitate prior to contact with the screw dislocation, as evidenced by the fact that the outer layers of the precipitate at the precipitate/matrix interface maintain the original bcc structure. The transformation appears martensitic (or displacive) in nature, since no vacancies are observed within the precipitate or at the interface and the simulation temperature (10K) is too low for thermally-activated processes. As the dislocation loops around the precipitate and detaches, many of the transformed Cu atoms revert to the original structure (Fig. 10c). Then, as the dislocation subsequently glides beyond the precipitate, nearly all of the transformed Cu atoms return to the original structure (Fig. 10d), even as the Orowan glide loop remains. On the other hand, a significant fraction of the transformed Cu atoms in the 4 nm diameter precipitate remain stable, even after the screw dislocation detaches by the Orowan mechanism. In the case of an edge dislocation interaction with a 2.5 nm diameter Cu precipitate, only a very small fraction of Cu atoms exhibit a similar transformation behavior. Therefore, the difference in the bypass mechanism observed for the screw and edge dislocation interaction with a 2.5 (and 4) nm diameter Cu precipitate must be due to the internal structural transformation. In other words, the (reversible) coherency loss within the precipitate increases the resistance to screw dislocation glide which induces the Orowan bypass mechanism.

In order to test whether this martensitic transformation is induced only by the presence of a screw dislocation, MD simulations without an applied shear stress were performed with a screw dislocation placed near a 1 to 4 nm diameter bcc Cu precipitate. No transformation was observed within the precipitate. As well, MD simulations have been performed with an applied shear stress, but without a screw dislocation. In this case, a transformation is observed for precipitate diameters of 1.8 nm and larger, but the transformation occurs at much higher applied shear stresses, namely 2,000, 1,250 and 1,000 MPa for the 1.8, 2.5 and 4 nm diameter Cu precipitates, respectively. These applied shear stress levels should be compared to the critical shear stress of about 625 MPa, irrespective of precipitate size, when the simulation is performed with a screw dislocation. Therefore, it can be concluded that the presence of a nearby screw dislocation assists the stress-induced transformation of a coherent bcc Cu precipitate.

The martensitic transformation within the precipitate is apparently driven by the superposition of the applied shear stress with the shear stress field of the screw dislocation. Continuum theory specifies that the maximum shear stress from a screw dislocation on the $(\bar{1}10)$ plane in the $[\bar{1}\bar{1}0]$ direction that drives the transformation, is about 82% of the maximum shear stress component ($\sigma_{ZY} = \frac{Gb}{2\pi d}$), where G, b and d are the shear modulus, the magnitude of the Burgers vector and the distance away from the dislocation core, respectively. For an edge dislocation, the shear stress field on the $(1\bar{1}0)$ plane in the $[\bar{1}\bar{1}0]$ direction is negligible, which in

conjunction with the lower applied stresses necessary for edge dislocation motion, explains why the transformation is not greatly assisted by an edge dislocation. The spatial dependence of the stress field around a screw dislocation can also explain why the transformed Cu atoms in the 2.5 nm precipitate revert to the original bcc lattice as the screw dislocation loops around and detaches from the Cu precipitate by the Orowan mechanism.

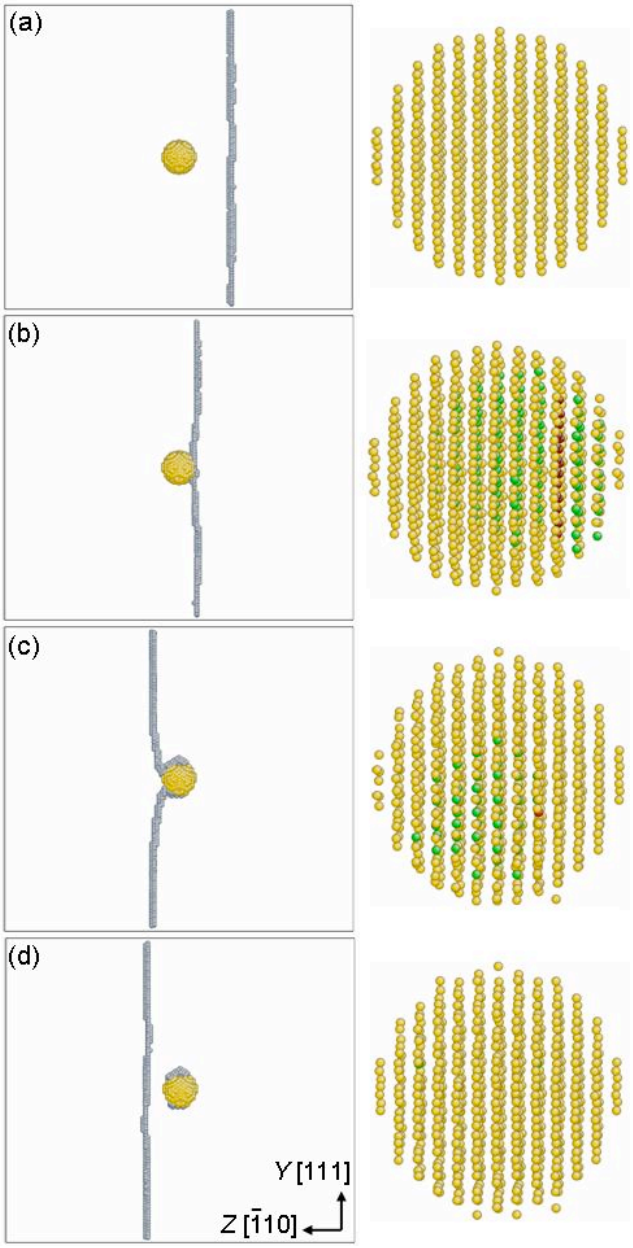

Figure 10. Snapshots in time from the MD simulation of the interaction between a screw dislocation and a 2.5 nm diameter bcc Cu precipitate with an applied shear stress of 1,000 MPa at (a) 12, (b) 27, (c) 53, and (d) 60 ps. The configurations on the left side show the entire dislocation line and precipitate, while the snapshots on the right side show the corresponding atomic configurations of the precipitate. The gray balls represent atoms in the screw dislocation core, while the yellow, red, and green balls represent Cu atoms in the bcc, fcc and hcp structures, respectively.

D. Experimental Validation

As part of our collaboration with Professor I. Robertson's group at UIUC, *in-situ* transmission electron microscopy measurements have been performed to investigate the interaction between moving dislocations and stacking fault tetrahedron and partially dissociated Frank loops, in order to compare with the molecular dynamics results just presented. The direct comparison of the simulation and experimental research has been the subject of a number of publications[18-20], and will only be briefly summarized here.

In situ TEM straining specimens of dimensions 10mm × 2.9mm were cut from 99.999% cold-rolled strip of pure polycrystalline copper (250μm thick) and from 99.99% pure gold sheet (200μm thick). Holes to accommodate the pins in the straining stage were drilled in the ends of the tensile bars followed by polishing the surfaces to a 600-grit finish. The copper samples were annealed at 1023 K in a vacuum furnace for 2 hours, furnace cooled and then annealed at 1273 K for a period of 2-10 minutes and quenched into iced brine. This treatment produced a large grain structure with stacking-fault tetrahedra and faulted Frank loops throughout the grains. The central sections were thinned to electron transparency by twin-jet electropolishing in a solution of 33% nitric acid in methanol cooled to 253 K at a current density of 0.11A cm^{-2}. The gold specimens were subjected to a similar treatment: vacuum annealed at 673 K for 8 hours, heated to 1313 K in air for times ranging from 5 to 20 minutes and then quenched in a brine solution at a temperature of 252 K. As the size and density of SFT produced in the gold are sensitive to the hold time at the quench temperature, multiple hold times were tried, with 5 minutes producing the largest, most well formed SFT. Electron transparent foils were produced using a twin-jet electropolishing apparatus with an electrolyte of 10.63g of LiCl, 22.31g of $Mg(ClO_4)_2$, 850 ml methanol, and 150 ml 2-butoxyethanol that was cooled to 218 K and a current density of 0.12 A cm^{-2}.

Straining of the rapidly quenched specimens was performed in a JEOL 4000 EX TEM and the dislocation reaction processes were recorded via a Gatan TV-rate camera onto S-VHS videotape for later analysis on a digital video editing system. In producing the figures for this paper, individual frames from the videotapes have been captured, image processed, and reproduced. Although every effort was made to capture the critical events this is not always possible given the reaction rates. To aid interpretation of the figures, schematic diagrams illustrating the events are included.

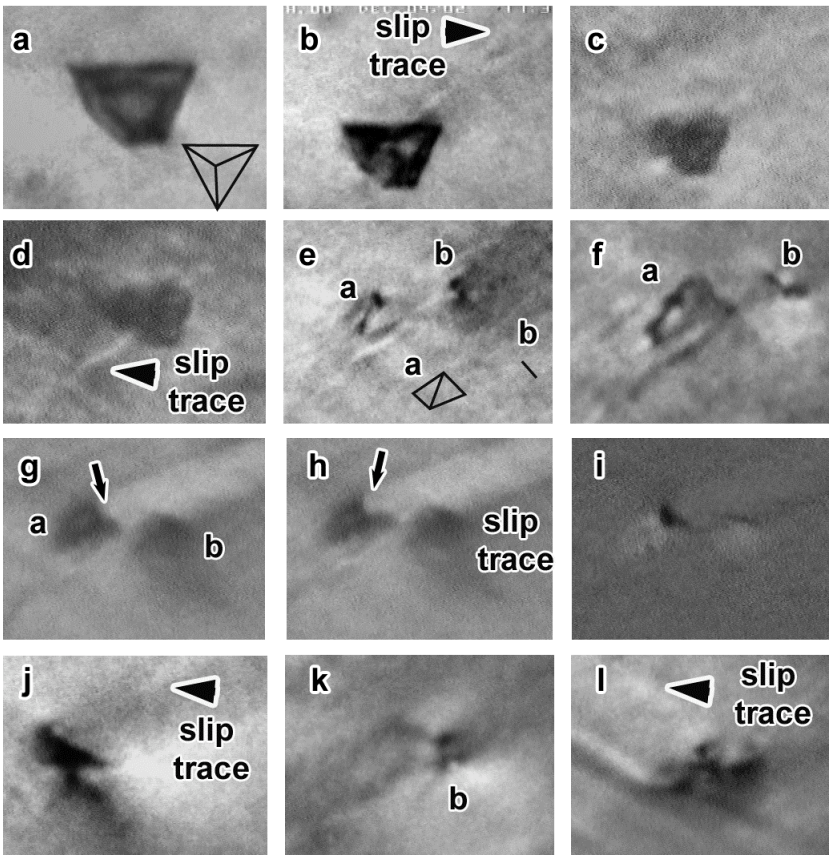

Figure 11. a-e The shearing of an SFT by a dislocation in gold and the subsequent formation of two new defects, *a* and *b*; g-h) interaction of another dislocation with the stacking fault tetrahedron, a; i is a difference image formed by superimposing a negative image of h on a positive image of g; j-l interaction of different slip dislocations with defect "b".

The series of images in Figures 11 show the interaction of glissile dislocations with stacking-fault tetrahedron in gold. The interaction with multiple dislocations results in the shearing, conversion, partial annihilation, and formation of stable resistant defect. A dislocation on a steeply inclined slip plane moves, as evidenced by the slip traces, from the upper right in Fig 11b and impacts the stacking fault tetrahedron. The dislocation shears the tetrahedron and is trapped at its edge, Fig. 11c, for several seconds before being released as shown by the slip trace extending from the tetrahedron in Fig.11d. The interaction with a second dislocation, not shown, converts the original tetrahedron into two defects, Figs. 11e-11g. One of these defects, labelled "*a"*, is a smaller tetrahedron. The nature of the other defect, labeled *"b"*, could not be ascertained. Although these defects appear well separated they reside at the extremes of the original defect. The impact of a dislocation with the small tetrahedron, "a", results in a change in the structure of one side of the tetrahedron; compare Figs. 11g and 11h. To highlight this difference, a comparison image has been created by superimposing a negative image of Fig. 11h on a positive image of Fig. 11g. The configurational change is seen as the dark region in Fig. 11i. Defect *b* is not impacted significantly as this dislocation does not intersect it. With time the small tetrahedron collapses into a glissile loop that moves away. The loss of this defect is evident in the series of images presented in Figures 11j-l, which show further dislocation interactions with defect *b* as additional displacement is applied. Although the dislocation interactions are difficult to discern in these images, the slip traces eventually extend on the opposite side of the defect. Unlike in the previous case, this defect remains a strong and

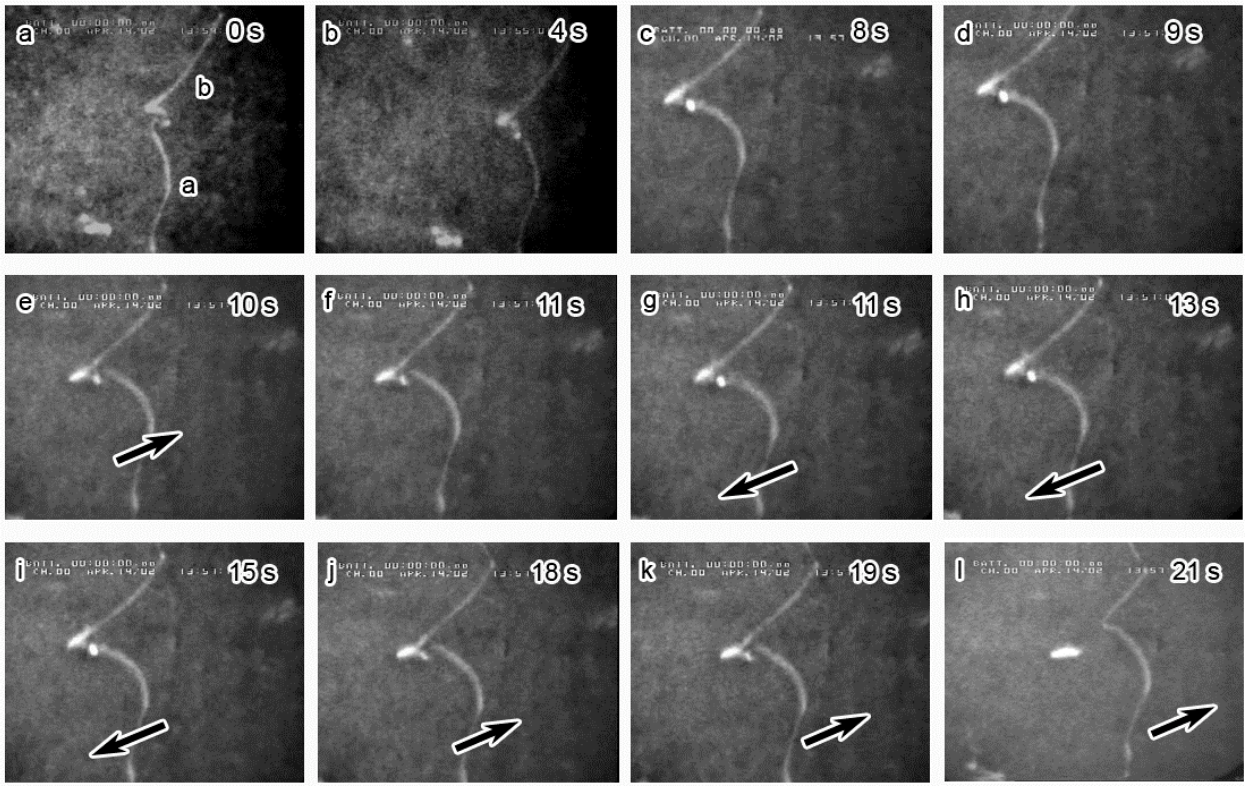

Figure 12. Weak-beam dark-field images showing the interaction of a dislocation with a stacking fault tetrahedron in copper. The arrows indicate the direction of motion of the dislocation, and the letters (*a* and *b*) the dislocation segments on either side of the stacking fault tetrahedron.

persistent barrier despite interacting with several different types of dislocations as noted by the different slip planes operating.

The images presented in Fig. 12 show a selection of weak-beam dark-field images of the interaction between a glissile lattice dislocation and a partially dissociated Frank loop (truncated SFT) in copper; the direction of motion of the dislocation is indicated by the arrow. Only the dislocation segment labeled "*a*" moves whereas segment "*b*" remains trapped. Segment *a* repeatedly moves forward but lacks sufficient inertia to break free of the defect and is pulled back toward the original position. This oscillation in position can be seen by comparing the dislocation positions in Figs. 12e and 12g and also in Figs. 12g and 12j. Finally, the dislocation breaks away and produces a jog in the dislocation and leaves behind a defect, Fig. 12l. Although the Burgers vector and nature of the resulting defect was not determined, it later slipped out of the foil. The loss of the loop may be a consequence of the proximity to the free surface. These observations suggest that the interaction results in conversion of the original defect from a faulted to a glissile loop, but not its direct annihilation. As the loop will present a different obstacle strength from the stacking-fault tetrahedron, any model will need to include this possibility if the probability for such a conversion is high.

IV. Summary

Molecular dynamics simulations have been used to investigate the atomic-scale interactions between gliding dislocations with defect clusters and precipitates in FCC and BCC model materials. The results are able to determine the obstacle strengths, including the observation of new interaction/strengthening mechanisms, and provide insight into the localized deformation in the form of defect free channels observed in irradiated structural materials. The modeling observations have been closely coordinated and compared with in-situ transmission electron microscopy studies performed in the group of Prof. Ian Robertson at the University of Illinois.

Molecular dynamics simulations of the interaction between edge, screw or mixed dislocations and a SFT show that the SFT is a strong barrier to dislocation motion. Further, these observations lead to the conclusion that dislocation channel formation is much more complicated than defect absorption in a single interaction, and may result from a combination of i) decreased defect cluster size due to shear, ii) partial absorption leaving isolated vacancies and smaller defect clusters of presumably reduced obstacle resistance, and iii) partial to complete absorption and the subsequent dragging and re-emission of defect clusters at a different location.

The precipitate resistance of copper precipitates to screw dislocation glide in BCC Fe depends strongly on precipitate size. The stress field of a screw dislocation assists the reversible transformation of bcc Cu precipitates larger than 1.8 nm diameter into a close-packed, but partially coherent structure in bcc Fe. These transformed precipitates are substantially stronger obstacles to dislocation glide, and can result in screw dislocation bypass by Orowan looping around the precipitate Whereas screw dislocation bypass of Cu precipitates with diameter larger than 2.5 nm occurs by an Orowan mechanism, the edge dislocation is always observed to bypass by the expected shear mechanism.

V. References

[1] Wirth BD, Odette GR, Marian J, Ventelon L, Young-Vandersall JA, and Zepeda-Ruiz LA, in *Multiscale modeling of radiation damage in fe-based alloys in the fusion environment*, Kyoto, Japan, 2004 (Elsevier, Amsterdam, Netherlands), p. 103.

[2] Bailat C, Almazouzi A, Baluc N, Schaublin R, Groschel F, and Victoria M, J. Nucl. Mater. **283-287,** 446 (2000).

[3] Bailat C, Groschel F, and Victoria M, J. Nucl. Mater. **276,** 283 (2000).

[4] Baluc N, Schaublin R, Bailat C, Paschoud F, and Victoria M, J. Nucl. Mater. **283-287,** 731 (2000).

[5] Garner FA, J. Nucl. Mater. **205,** 98 (1993).

[6] Garner FA and Toloczko MB, J. Nucl. Mater. **206,** 230 (1993).

[7] Linga Murty K, J. Nucl. Mater. **270,** 1 (1999).

[8] Lucas GE, J. Nucl. Mater. **206,** 287 (1993).

[9] Lucas GE, J. Nucl. Mater. **216,** 322 (1994).

[10] Mansur LK and Bloom EE, **34,** 23 (1982).

[11] Victoria M, Baluc N, Bailat C, Dai Y, Luppo MI, Schaublin R, and Singh BN, J. Nucl. Mater. **276,** 114 (2000).

[12] Robach JS, Robertson IM, Wirth BD, and Arsenlis A, Phil. Mag. **83,** 955 (2003).

[13] Arsenlis A, Wirth BD, and Rhee M, Phil. Mag. **84,** 3617 (2004).

[14] Y. Mishin, M.J. Mehl, D.A. Papaconstantopoulos, A.F.Voter, and J.D. Kress, Phys. Rev. B **63** (22), 224106 (2001).

[15] G. J. Ackland, D. J. Bacon, A. F. Calder, and T. Harry, Philos. Mag. A **75**, 713 (1997).

[16] Rodney D, Acta Materialia 52 (3): 607-614 FEB 9 2004.

[17] Weertman J, Weertman JR, Elementary Dislocation Theory, Oxford University Press, 1992.

[18]

[19]

[20] I.M. Robertson, B.D. Wirth, M. Briceno and J. Fenske, Transaction of the American Nuclear Society **96** (2008) 24-28.

V. Appendix

Peer reviewed publications:

1. H.-J. Lee, J.-H. Shim and B.D. Wirth, "A molecular dynamics simulation of screw dislocation interaction with stacking fault tetrahedron in FCC Cu", *J. Mater. Research* **22** (2007) 2758 – 2769.
2. H.-J. Lee, J.-H. Shim, and B.D. Wirth, "Molecular Dynamics Simulation of Dislocation – Obstacle Interactions in Irradiated Materials", *Key Engineering Materials* **345-346** (2007) 947.
3. L. Saintoyant, H.-J. Lee and B.D. Wirth, "Molecular dynamics study of the interactions between dislocations and imperfect stacking fault tetrahedron in Cu", *J. Nucl. Mater* **361** (2007) 206.
4. J.-H. Shim, Y.W. Cho, S.C. Kwon, W.W. Kim, and B.D. Wirth, "Screw dislocation assisted martensitic transformation of a bcc Cu precipitate in bcc Fe", *Appl. Physics Lett.* **90** (2007) 021906.
5. J.S. Robach, I.M. Robertson, H.-J. Lee, and B.D. Wirth, "Dynamic observations and atomistic simulations of dislocation – defect interactions in rapidly quenched copper and gold", *Acta Mat* **54** (2006) 1679.
6. I.M. Robertson, A. Beaudoin, K. Al-Fadhalah, Li. Chun-Ming, J. Robach, B.D. Wirth, A. Arsenlis, D. Ahn and P. Sofronis, "Dislocation – obstacle interactions: dynamic experiments to continuum modeling", *Materials Science and Engineering A* **400-401**(2005) 245.
7. P. Jing, T. Khraishi, J.A. Young and B.D. Wirth, "Multi-scale simulations of the effects of irradiation-induced voids and helium bubbles on the mechanical properties of aluminum", *Philosophical Magazine* **85** (2005) 757.
8. I.M. Robertson, B.D. Wirth, M. Briceno and J. Fenske, "Dislocation – radiation obstacle interactions: developing improved mechanical property constitutive models", Transaction of the American Nuclear Society **96** (2008) 24-28.
9. B.D. Wirth, H.-J. Lee, and I.M. Robertson, "Atomistic Simulations of Dislocation Interaction with Staking Fault Tetrahedra", OECD Structural Materials for Innovative Nuclear Systems Conference (2007), *in press*.